POAC'25
St. John's, Newfoundland and Labrador, Canada

Proceedings of the 28th International Conference on Port and Ocean Engineering under Arctic Conditions
Jul 13-17, 2025
St. John's, Newfoundland and Labrador
Canada

Spatio-temporal analysis of flow around slip airfoils

Eugene Kankam [1], Emmanuel Quayson-Sackey [1], Baafour Nyantekyi-Kwakye[1]
[1]Dalhousie University, Nova Scotia, Canada

ABSTRACT

The present study investigates the impact of slip boundary conditions, implemented using superhydrophobic coatings (SHC), on the aerodynamic performance and wake dynamics of an airfoil. Using numerical simulations, we compare the effects of slip lengths (L_s = 100 μm, 140 μm, and 185 μm) with the no-slip baseline case. Results demonstrate that slip conditions reduce skin friction by up to 25%, suppress flow separation, and accelerate wake recovery. The observed suppression of recirculation zones and faster boundary layer recovery suggest SHC could mitigate ice formation by reducing droplet retention and disrupting stagnation regions. Wavelet analysis of wake fluctuations reveals that slip conditions redistribute energy from low frequencies ($f \approx 8$ –12 Hz) to higher frequencies ($f \approx 20 - 50$ Hz), disrupting large-scale vortex formation and promoting earlier turbulence onset. The findings highlight the dual potential of SHC in enhancing flow stability and drag reduction while providing passive anti-icing benefits, particularly for offshore wind turbine (OWT) applications where icing significantly impacts performance.

KEY WORDS: Offshore wind turbine; superhydrophobic coating; turbulence; wavelet analysis wake dynamics.

INTRODUCTION

The transition from fossil fuels to renewable energy has accelerated due to environmental concerns, technological advancements, and policy shifts. Climate change, driven by fossil fuel emissions, has prompted global efforts to reduce greenhouse gas emissions (Hinrichs-Rahlwes, 2024). Renewable energy technologies, particularly wind power, have seen significant growth, with global wind generation increasing by 14% in 2022 (International Energy Agency, 2023). However, to meet the Net Zero Emissions by 2050 target, wind power must achieve approximately 7,400 TWh by 2030.

Until recent years, wind turbines were primarily installed in coastal areas with milder climates, where considerations for extreme cold, freezing rain, or icing were not critical. Offshore wind farms, especially in cold regions, offer promising potential due to higher air density and enhanced energy capture (Wei et al., 2020;Tahir et al., 2021). However, designing and installing OWT remains challenging, as atmospheric ice accumulation on blades severely impacts aerodynamic performance and structural integrity (Etemaddar et al., 2014). However, ice accumulation on turbine blades poses significant challenges, reducing aerodynamic efficiency and energy production by up to 30% (Battisti, 2015). To address this, researchers have explored active and passive mitigation techniques. Active methods, such as heating, require significant energy, while passive methods, like hydrophobic coatings, offer energy-efficient solutions with lower operational costs (Madi et al., 2019; Quayson-Sackey et al., 2025). Among the passive methods, SHC have drawn significant attention due to their characteristics. Their low surface energy and micro/nano-scale surface roughness creates a high contact angle and low contact angle hysteresis for water droplets leading to low friction at the

liquid-solid interface (Lee et al., 2016). This slippage effect reduces drag, benefiting engineering applications involving fluid transport and flow efficiency.

Recent studies have investigated the impact of SHC on unsteady flow dynamics around airfoils. Mallah et al., 2021 studied the impact of SHC on a NACA 0012 airfoil in a water tunnel at low Reynolds number (Re = 2400). The authors applied proper orthogonal decomposition (POD) technique to the flow field and observed SHC-induced shifts in energy distribution. SHC induced earlier transitions to symmetric wakes, enhancing thrust by 13%. Sooraj et al. (2019, 2020) explored SHC effects on cylinders and hydrofoils across a range Re = 45 – 15,500. They observed elongated shear layers, weakened wake turbulence, and enhanced coherent structures. Lee et al. (2018) investigated the effects of SHC on a NACA0012 hydrofoil and observed reduced vortex formation length and upstream shifts in Reynolds stress peaks, further supporting SHC potential for flow stabilization.

Numerical simulations are usually used to complement experimental findings and improve optimization techniques. Shahsavari et al. (2023) used Reynolds-Averaged Navier-Stokes (RANS) simulations to model external flow over a superhydrophobic hydrofoil at Re = 10^5 and analyzed the effects of slip lengths and angles of attack on lift coefficients (C_l). They observed that C_l did not always increase monotonically with slip length while drag consistently decreased. Mollicone et al. (2022) also used the spectral element method to model turbulent flow over a bluff body where alternating no-slip and shear-free boundary conditions were used to simulate gas pockets. Simulations analyzed effects on separation and reattachment points and drag forces. The superhydrophobic surface (SHS) patterns increased turbulence production in the shear layer near the wall, delaying separation and advancing reattachment, which reduced the size of the separation bubble by up to 35%. SHS-induced vortical structures anchored at the no-slip/shear-free interfaces increased velocity fluctuations and promoted earlier pressure recovery. Huang et al. (2018) also demonstrated that higher slip lengths delayed vortex shedding and stabilized wake flow.

Despite significant progress, existing studies have primarily relied on methods like POD or spectral analysis to identify flow structures and turbulence characteristics. While POD provides a compact representation of complex flow fields, it has limitations in capturing transient and non-stationary behaviors, as it averages the flow over the entire domain, losing critical time-dependent features. Spectral analysis allows for the identification of periodic components and their energy distribution across various scales. However, spectral analysis assumes stationarity, meaning that the statistical properties of the signal do not change over time. This assumption is problematic when dealing with turbulent flows, which are often non-stationary and contain transient bursts of energy that Fourier transforms tend to smooth out. Spectral analysis may not fully capture the dynamic nature of the turbulence, especially when the flow exhibits sudden changes or highly intermittent events.

Therefore, the present study investigates the flow dynamics around an airfoil under different slip boundary conditions. A wavelet analysis is employed to examine the unsteady and transient characteristics of the wake, offering insights into turbulence dynamics and energy distribution that complement the other flow metrics.

SIMULATION SETUP

Numerical algorithm and simulation setup

The present study employs the Unsteady Reynolds-Averaged Navier-Stokes (URANS) equations to model turbulent flow. The governing equations consist of the continuity and momentum equations:

$$\frac{\partial \rho}{\partial t} + \nabla \cdot (\rho U) = 0 \tag{1}$$

$$\frac{\partial(\rho U)}{\partial t} + \nabla \cdot (\rho UU) = -\nabla p + \nabla \cdot [(\mu + \mu_t)(\nabla U + (\nabla U)^T)] - \nabla \cdot \rho\overline{u'u'} \tag{2}$$

where ρ is the fluid density, U is the velocity vector, p is the pressure, μ is the dynamic viscosity, μ_t is the turbulent viscosity, and $\overline{u'u'}$ represents the Reynolds stress tensor. The additional transport equations required for turbulence closure are solved using the Shear Stress Transport (SST) k-ω model, which blends the k-ε and k-ω formulations. The SST model is chosen due to its ability to accurately predict turbulence effects in both the near-wall region and the freestream. The transport equations for the turbulent kinetic energy (k) and the specific turbulence dissipation rate (ω) are expressed as:

$$\frac{\partial(\rho k)}{\partial t} + \nabla \cdot (\rho Uk) = \nabla \cdot \left[\left(\mu + \frac{\mu_t}{\sigma_k}\right)\nabla k\right] + P_k - \rho\beta^* k\omega \tag{3}$$

$$\frac{\partial(\rho\omega)}{\partial t} + \nabla \cdot (\rho U\omega) = \nabla \cdot \left[\left(\mu + \frac{\mu_t}{\sigma_\omega}\right)\nabla\omega\right] + \gamma\frac{P_k}{\nu_t} - \beta\rho\omega^2 + 2(1 - F_1)\frac{\rho\sigma_{\omega 2}}{\omega}\nabla k \cdot \nabla\omega \tag{4}$$

The production term for turbulent kinetic energy is given by $P_k = 2\mu_t S_{ij} S_{ij}$ where the strain rate tensor is defined as:

$$S_{ij} = \frac{1}{2}\left(\frac{\partial U_i}{\partial x_j} + \frac{\partial U_j}{\partial x_i}\right) \tag{5}$$

The turbulent eddy viscosity is computed as:

$$\mu_t = \frac{a_1 \rho k}{\max(a_1\omega, SF_2)} \tag{6}$$

where $S = \sqrt{2S_{ij}S_{ij}}$ is the mean strain rate magnitude. To account for wall effects and improve prediction in separated flows, the blending function F_1 is defined as:

$$F_1 = \tanh\left(\left(\min\left[\max\left(\frac{\sqrt{k}}{\beta^*\omega d}, \frac{500\nu}{d^2\omega}\right), \frac{4\rho\sigma_{\omega 2}k}{d^2}\right]\right)^4\right) \tag{7}$$

where d represents the distance to the closest wall. The SST formulation transitions smoothly between k-ω near the wall and k-ε in the freestream by modifying the turbulent eddy viscosity and introducing a viscosity limiter. This limiter prevents overprediction of eddy viscosity in regions of strong flow separation.

Test case, grid generation and boundary conditions

The study employed the NACA 64-618 airfoil, commonly used in the tip section of the NREL 5MW baseline OWT blade (Jonkman, 2009). This 6-series airfoil features a maximum thickness of 18%, located at 34.7% of the chord from the leading edge, and a maximum camber of 3.3% at 50% of the chord. The airfoil, with a chord length of c = 1 m, is positioned at the center of the computational domain, as depicted in Fig. 1(a). The domain extends 10c upstream from the airfoil leading edge, 22c downstream from the leading edge and spans $\pm$ 10c in the wall normal direction. This configuration ensures accurate capture of wake

development, vortex shedding, and prevents flow reversal at the outlet. The domain was discretized using a fully structured *C*-type mesh around the airfoil, as shown in Fig. 1(b).

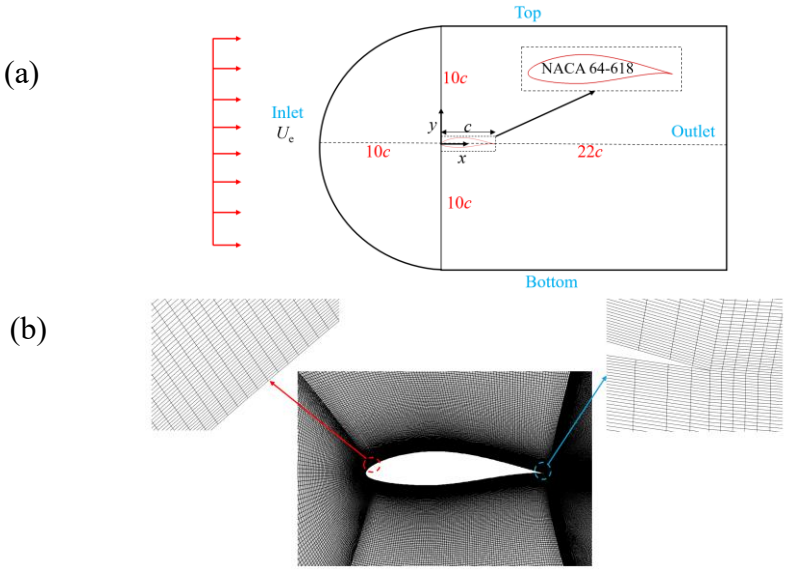

Figure 1. Schematic diagram of the (a) computational domain and (b) mesh distribution around the airfoil model.

The close-up view reveals that the mesh maintains good orthogonality near the airfoil surface, ensuring precise boundary layer resolution. To resolve regions with high velocity gradients and strong shear forces on the airfoil wall, the first node was placed 0.002 mm from the boundary, achieving a dimensionless wall distance (y^+) of less than 1. The cell size increased by a growth ratio of 1.2 away from the wall. A grid independence study was conducted to ensure mesh adequacy, resulting in a final mesh comprising approximately 750 × 10^3 cells. Air at 15 °C with density of ρ_{air} = 1.225 kgm^{-3} and constant dynamic viscosity of μ_{air} = 1.789 × 10^{-5} Pa/s was used as a working fluid. For boundary conditions, a uniform velocity of U_e = 20 m/s was prescribed at the inlet using a Dirichlet boundary condition, while a constant relative pressure of 0 Pa was applied at the outlet. Symmetry conditions were enforced at the top and bottom surfaces of the computational domain. To investigate the effect of slip on the wake dynamics of the airfoil at α =12°, two boundary conditions were applied. Initially, a no-slip boundary condition was assigned to the wall surfaces, setting zero velocity at the fluid-solid interface. Subsequently, a slip surface boundary condition was modeled using the Navier slip boundary condition, as shown in Eq. (8) to simulate a SHS (Navier, 1822)

$$U_s = L_s \frac{\partial U}{\partial n}\Big|_{wall} \tag{8}$$

The U_s at each cell on the airfoil surface was calculated by multiplying the tangential velocity gradient by the specified L_s. A user-defined function script was written and compiled using the in-built compiler in ANSYS FLUENT. Notably, U_s was determined iteratively by executing the equation with a low relaxation factor in each iteration. The resulting U_s was then used to modify the airfoil wall boundary condition in the software. The numerical simulations are performed using ANSYS FLUENT 2024 R1, employing the semi-implicit method for pressure-linked Equations algorithm for pressure-velocity coupling. A second-order implicit temporal discretization was adopted to improve accuracy in capturing transient turbulent structures. Spatial discretization was performed using a second-order upwind scheme, which reduces numerical diffusion and improves the resolution of turbulent structures. The time step

size was set to 3×10^{-4}s, determined based on a Courant-Friedrichs-Lewy condition analysis to ensure numerical stability while adequately resolving turbulent structures. All simulations were performed on the Beluga high-performance computing cluster, utilizing Intel Gold 6148 Skylake 2.4 GHz processors. The total computational time was about 300 CPU hours for the completion of flow field calculations and the collection of turbulence statistics. To ensure statistical convergence, the simulation initially run for 6 flow-through times, to allow the flow to reach a statistically stationary state. The collection of turbulence statistics was then carried out over an additional 5 flow-through times, ensuring the accumulation of sufficient time-averaged data for turbulence analysis

Validation

Due to the absence of direct reference data for the coated NACA 64-618 airfoil, a comparative analysis was performed using published results for the uncoated airfoil (Romani et al., 2018). The analysis primarily examines the mean pressure coefficient (C_p) distribution along the airfoil at $\alpha = -0.88°$. Figure 2(a) shows the C_p variation along the normalized chord length (x/c) at $\alpha = -0.88°$. The numerical results from this study exhibit strong alignment with experimental data across most of the chord length. However, a minor discrepancy is noted in the suction region near the airfoil's upper surface ($x/c = 0.6$) where the numerical results underestimate C_p by approximately 15%. This deviation may stem from limitations in the turbulence modeling approach, which struggles to fully capture complex boundary layer interactions in this region. Figure 2(b) depicts the variation of the lift coefficient (C_l) as a function of α, ranging from 0° to 12°. The numerical predictions closely match the wind tunnel results from results from Abbott and Von Doenhoff, (2012) , showing consistent trends across the tested angles. The lift coefficient increases linearly with α at lower angles but exhibits nonlinear growth at higher angles, particularly near $\alpha = 12°$. This nonlinearity signifies the onset of flow separation at higher angles, which the numerical approach accurately captures.

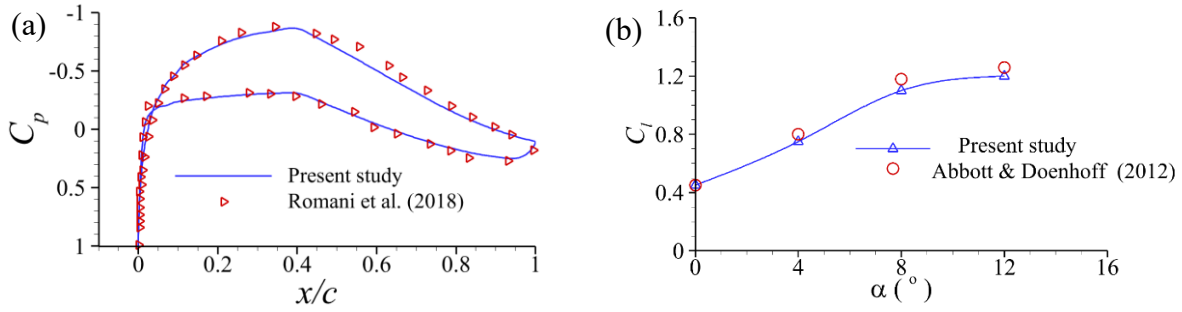

Figure 2. Comparison of (a) mean pressure and (b) lift coefficient of the present study with experimental data for no-slip boundary condition.

RESULTS AND DISCUSSION

Spanwise Vorticity

Figure 3 presents a spanwise vorticity distribution for different surface conditions, providing insights into the effect of slip on the wake dynamics at $\alpha = 12°$. In the no-slip case, strong vortex shedding is observed with well-defined alternating regions of positive and negative vorticity in the wake. The boundary layer on the suction side undergoes separation near the trailing edge, rolling up into large coherent structures downstream. This behavior is characteristic of Kármán vortex shedding, where the instability within the shear layer leads to

the formation of periodic vortices. The presence of these strong vortices suggests significant fluctuations in the aerodynamic loads, which could contribute to increased drag and unsteady forces on the airfoil. Under icing conditions, such flow instabilities would promote droplet impingement and ice accumulation.

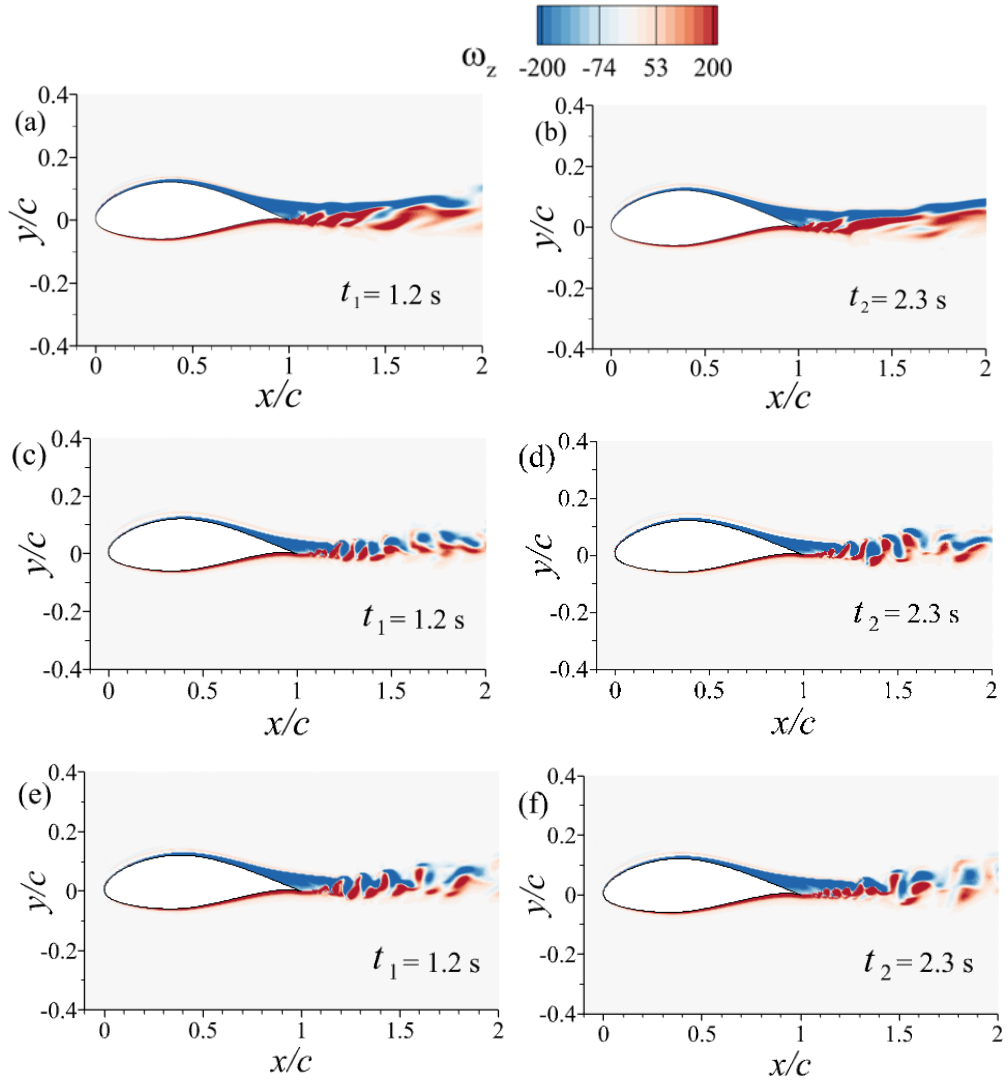

Figure 3. Contours of spanwise vorticity for the following boundary conditions: (a, b) no-slip, (c, d) L_s = 100 µm and (e, f) L_s = 140 µm. The snapshots are taken at two different time intervals: t_1 = 1.2 s and t_2 = 2.3 s

As slip increases, modifications to the wake structure become apparent. For L_s = 100 μm, the separated shear layer rolls up earlier than in the no-slip case, indicating that slip conditions promote earlier vortex formation. This behavior is consistent with previous studies that highlight a reduction in the recirculation region and a shift in the vortex shedding location. The reduced vorticity intensity in the wake suggests a mitigation of flow separation effects, leading to a potential decrease in aerodynamic drag. Such flow stabilization could prevent the formation of ice by maintaining more attached flow over the airfoil surface, reducing the recirculation zones where supercooled water droplets tend to accumulate and freeze. With L_s = 140 μm, the wake structure exhibits further changes. The vortices remain more compact, and the vortex formation length appears shorter than in the no-slip and L_s = 100 μm cases. This suggests an enhanced momentum exchange between the wake and the free stream, leading to

a quicker recovery of the velocity profile downstream. The reduction in vortex size and strength indicates that slip conditions are suppressing large-scale flow instabilities, which can contribute to improved aerodynamic efficiency. These modified flow characteristics may significantly reduce ice formation by minimizing surface flow separation, decreasing droplet residence time on the airfoil surface, and preventing the formation of stagnation zones where ice typically initiates. The more stable flow conditions created by slip surfaces could therefore serve as a passive anti-icing mechanism by altering the fundamental flow physics that enable ice accretion.

Mean flow field

The contours of the normalized streamwise mean velocities (U/U_e) for all test cases are shown in Fig. 4. The flow topology indicates typical aerodynamic behavior, with flow deceleration near the leading edge, acceleration along the suction surface of the airfoil, and separation at the trailing edge due to the adverse pressure gradient formed by the upstream flowing fluid.

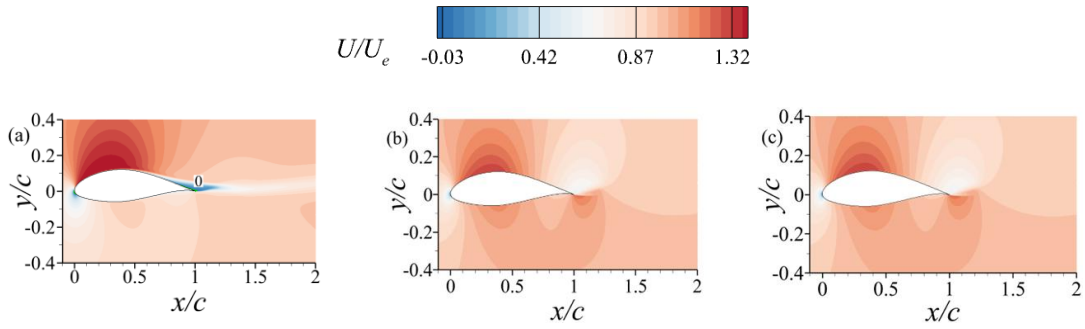

Figure 4. Contours of mean streamwise velocities for (a) no-slip (b) L_s = 100 μm and (c) L_s = 140 μm.

For the no-slip case as shown in Figure 4 (a), a distinct reverse flow region ($U < 0$) is observed near the trailing edge on the suction surface, demarcated by the zero-contour line ($U = 0$). This is accompanied by a recirculation bubble characterized by counterclockwise rotating vortices, as seen in the mean streamlines. This reversal of flow near the trailing edge is indicative of flow separation caused by the adverse pressure gradient, a condition that could cause ice accretion by creating stagnation regions where supercooled droplets can accumulate and freeze. In contrast, for the slip boundary conditions as shown in Figures 4(b) and 4(c), the boundary layer remains attached to the surface, and flow separation is notably suppressed. The slip condition introduces a non-zero slip velocity, which helps overcome the adverse pressure gradient, thereby reducing the formation of the recirculation bubble. This behavior leads to less flow deceleration in comparison to the no-slip case. Such characteristics directly inhibit ice formation by minimizing surface regions prone to droplet stagnation and by maintaining higher surface velocities that reduce water droplet residence time. Interestingly, the flow field for the two slip cases appears similar, suggesting that the influence of slip length on the wake dynamics may be relatively small within the tested range. This implies that even modest slip conditions (L_s =100μm) may provide significant benefits for ice prevention by maintaining attached flow.

Skin Friction and Pressure Distribution

The distributions of the skin friction coefficient **(C_f)** and pressure coefficient **(C_p)** along the airfoil surface are presented in Figure 5 to provide insight into the effects of slip boundary conditions on boundary layer development and aerodynamic forces. The C_f

distribution indicates that for the no-slip case, skin friction is highest near the leading edge due to the strong velocity gradients in the boundary layer and decreases downstream as the boundary layer thickens. This high friction region corresponds to where ice typically first accumulates on airfoils. The introduction of slip conditions (L_s = 100, 140, and 185 μm) significantly reduces skin friction, particularly in the mid-chord region, where lower values suggest weaker wall shear stress and a modified boundary layer evolution. The C_p distribution highlights modifications in the surface pressure distribution due to slip. The no-slip case exhibits a strong adverse pressure gradient on the suction side, contributing to flow separation. With slip conditions, the pressure distribution shifts, reducing the suction peak and delaying the pressure recovery. The overlapping nature of the slip cases indicates that beyond a certain threshold ($L_s \geq$100 μm), further increases in slip length do not significantly alter the pressure distribution. This suggests a saturation effect where additional slip does not lead to further aerodynamic benefits in terms of pressure recovery, which may correspond to a limiting effect on ice prevention as well.

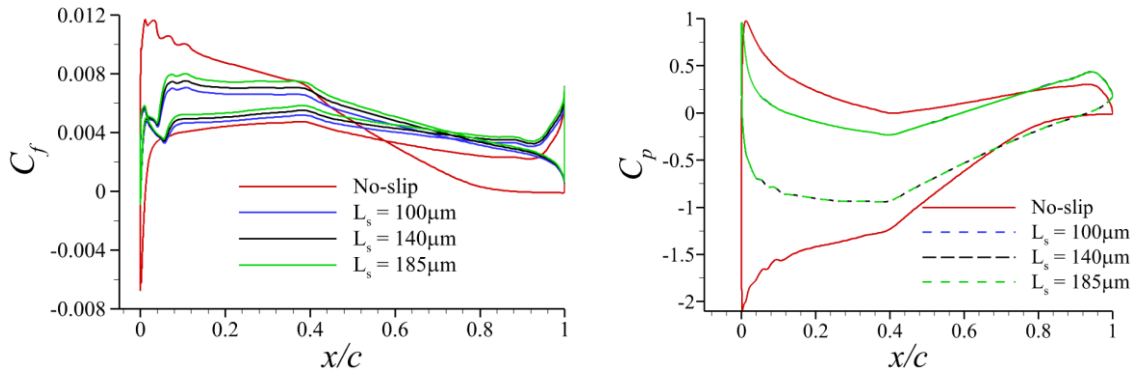

Figure 5. Distributions of C_f and C_p along the airfoil surface for different boundary conditions: (a) no-slip (b) L_s = 100 μm and (c) L_s = 140 μm.

Wavelet analysis

The wavelet analysis presented in Figure 6 compares the spectral characteristics of velocity fluctuations in the wake of an airfoil under no-slip and slip boundary conditions. For the probe closest to the trailing edge, the no-slip case exhibits strong energy concentrations at low frequencies ($f \approx$ 10 Hz), indicative of large-scale coherent structures associated with periodic vortex shedding. These persistent, well-defined wake dynamics would promote ice accretion by creating regular pressure fluctuations that enhance droplet impingement and by maintaining stable recirculation zones where water can accumulate and freeze. Figure 6(b), however, shows a more fragmented distribution of energy, with reduced intensity at lower frequencies. This suggests that slip conditions modify vortex formation, potentially delaying or weakening large-scale shedding while allowing higher-frequency fluctuations to emerge. Such modified wake dynamics could disrupt the formation of ice ridges by preventing the establishment of stable flow separation patterns that typically serve as nucleation sites for ice accumulation.

Moving downstream, the spectral distribution changes significantly. Figure 6(c) maintains energy concentrations at low frequencies, though the intensity begins to diminish as vortices break down and turbulence develops. Figure 6(d), in contrast, exhibits a broader frequency distribution with increased intermittency, suggesting a shift in turbulence dynamics.

The presence of multiple energetic bursts at varying frequencies indicates that the slip condition affects wake evolution, leading to more chaotic flow structures.
Further downstream (Figures 6(e) and 6(f)) shows a continued decay of energy, but with very little distinct differences between the two cases. Figure 6(e) retains some residual low-frequency structures, although the wake becomes increasingly diffuse. Figure 6(f)**,** however, exhibits a more distributed energy spectrum with less pronounced coherent structures. This suggests that slip accelerates the transition to smaller-scale turbulence, possibly due to reduced shear-layer interaction.

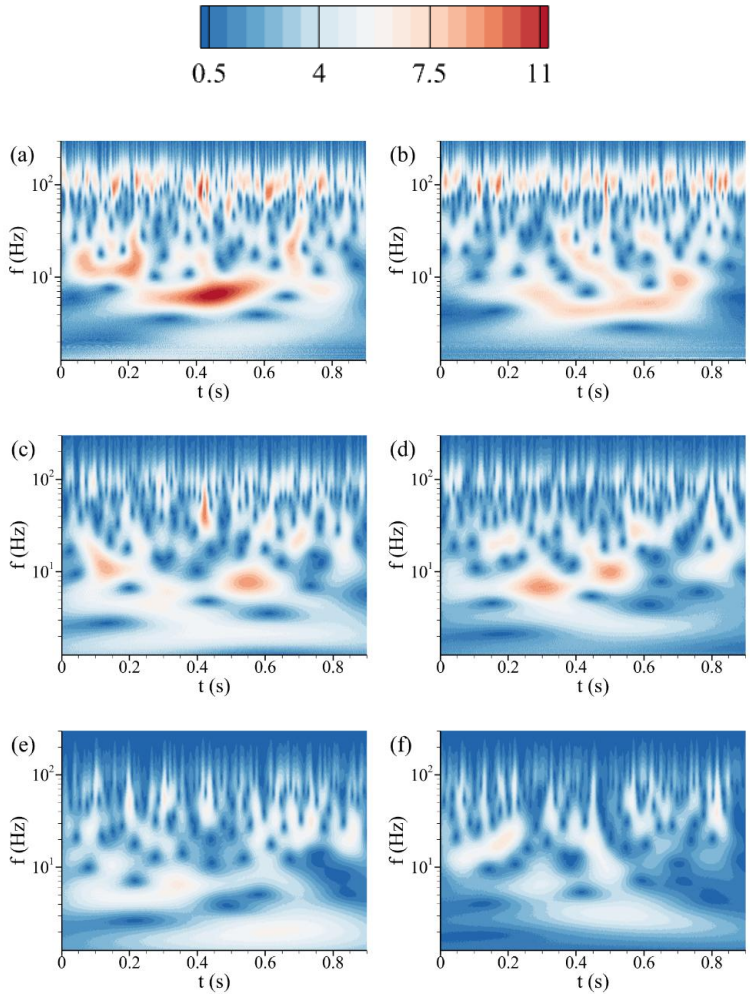

Figure 6. Wavelet transforms the velocity fluctuations in the wake for various boundary conditions at different time intervals. The left column (a, c, e) corresponds to the no-slip case, while the right column (b, d, f) represents the slip conditions. The first row (a, b) represents the probe at x = 1.5 m, (c, d) at x = 1.8 m, and (e, f) at x = 2.3 m.

CONCLUSIONS

This study investigates the effects of slip boundary conditions on the aerodynamic performance and wake dynamics of an airfoil, with particular emphasis on drag reduction and flow separation suppression. The results demonstrate that the introduction of slip conditions, particularly through superhydrophobic coatings (SHC), significantly alters the boundary layer characteristics and wake behavior compared to the no-slip case, while simultaneously revealing it's potential for ice prevention.
The mean velocity field analysis reveals that slip conditions maintain a more attached boundary layer, suppressing the formation of recirculation bubbles near the trailing edge and reducing

flow separation. The wake region under slip conditions exhibits faster velocity recovery, attributed to the enhanced entrainment of ambient fluid, which leads to a more efficient mean flow recovery. This potentially reduces water droplet residence time on the surface. However, further increases in slip length show diminishing returns, as the flow fields for the slip cases become similar beyond $L_s = 100\mu m$. The skin friction and pressure distributions confirm these findings, with slip conditions significantly reducing wall shear stress and altering the pressure gradient along the airfoil surface. The reduced adverse pressure gradient indicates a suppression of flow separation, which can enhance aerodynamic performance, particularly in terms of drag reduction and improved lift characteristics. These benefits are most prominent at higher slip lengths, though the results suggest a saturation effect where additional increases in slip length do not provide further aerodynamic advantages.

Wavelet analysis of velocity fluctuations in the wake further corroborates the impact of slip conditions on wake dynamics. Slip boundaries disrupt the formation and persistence of large-scale coherent structures, redistributing energy towards higher frequencies and promoting earlier breakdown into turbulence. This shift in the spectral characteristics suggests that slip boundary conditions can play a crucial role in optimizing wake behavior for improved aerodynamic stability and drag reduction while creating surface flow conditions less conducive to stable ice accumulation. The modified turbulence characteristics may particularly help prevent the formation of spanwise-ice ridges that typically follow coherent vortex shedding patterns.

ACKNOWLEDGEMENTS

The authors acknowledge financial support from National Sciences and Engineering Research Council of Canada Discovery grant (RGPIN-2024-04606) awarded to BN-K and the support of Digital Research Alliance of Canada.

REFERENCES

Abbott, I. H., & Von Doenhoff, A. E. (2012). *Theory of wing sections: including a summary of airfoil data*. Courier Corporation.

Battisti, L. (2015). *Wind Turbines in Cold Climates Icing Impacts and Mitigation Systems*. Springer.

Etemaddar, M., Hansen, M. O. L., & Moan, T. (2014). Wind turbine aerodynamic response under atmospheric icing conditions. *Wind Energy*, *17*(2), 241–265. https://doi.org/10.1002/we.1573

Hinrichs-Rahlwes, R. (2024). Renewable Energy for Climate Protection and Energy Security: Lessons Learned from the European Green Deal and REPowerEU. *Transition Towards a Carbon Free Future: Selected Papers from the World Renewable Energy Congress (WREC) 2023*, 245–257.

Huang, H., Liu, M., Gu, H., Li, X., Wu, X., & Sun, F. (2018). Effect of the slip length on the flow over a hydrophobic circular cylinder. *Fluid Dynamics Research*, *50*.

International Energy Agency, I. (2023). *World Energy Outlook 2023*. www.iea.org/terms

Jonkman, J. (2009). Definition of a 5-MW Reference Wind Turbine for Offshore System Development. *National Renewable Energy Laboratory*.

Lee, C., Choi, C. H., & Kim, C. J. (2016). Superhydrophobic drag reduction in laminar flows: a critical review. *Experiments in Fluids*, *57*(12). https://doi.org/10.1007/s00348-016-2264-z

Lee, J., Kim, H., & Park, H. (2018). Effects of superhydrophobic surfaces on the flow around an NACA0012 hydrofoil at low Reynolds numbers. *Experiments in Fluids*, *59*(11). https://doi.org/10.1007/s00348-018-2564-6

Madi, E., Pope, K., Huang, W., & Iqbal, T. (2019). A review of integrating ice detection and mitigation for wind turbine blades. In *Renewable and Sustainable Energy Reviews*, 103, 269–281). https://doi.org/10.1016/j.rser.2018.12.019

Mallah, S. R., Sooraj, P., Sharma, A., & Agrawal, A. (2021). Effect of superhydrophobicity on the wake of a pitching foil across various Strouhal numbers. *Physics of Fluids*, *33*(11). https://doi.org/10.1063/5.0068088

Mollicone, J. P., Battista, F., Gualtieri, P., & Casciola, C. M. (2022). Superhydrophobic surfaces to reduce form drag in turbulent separated flows. *AIP Advances*, *12*(7). https://doi.org/10.1063/5.0098365

Navier, C. (1822). *Mémoire sur les lois du mouvement des fluides*. éditeur inconnu.

Quayson-Sackey, E., Nyantekyi-Kwakye, B., & Ayetor, G. K. (2025). Technological advancements for anti-icing and de-icing offshore wind turbine blades. In *Cold Regions Science and Technology* 231. https://doi.org/10.1016/j.coldregions.2024.104400

Romani, G., van der Velden, W. C., & Casalino, D. (2018). Deterministic and statistical analysis of trailing-edge noise mechanisms with and without serrations. *2018 AIAA/CEAS Aeroacoustics Conference*, 3129.

Shahsavari, A., Nejat, A., Climent, E., & Chini, S. F. (2023). Unexpected trends of lift for hydrofoils with superhydrophobic coating. *European Journal of Mechanics, B/Fluids*, *101*, 219–226. https://doi.org/10.1016/j.euromechflu.2023.05.004

Sooraj, P., Jain, S., & Agrawal, A. (2019). Flow over hydrofoils with varying hydrophobicity. *Experimental Thermal and Fluid Science*, *102*, 479–492. https://doi.org/10.1016/j.expthermflusci.2018.12.021

Sooraj, P., Ramagya, M. S., Khan, M. H., Sharma, A., & Agrawal, A. (2020). Effect of superhydrophobicity on the flow past a circular cylinder in various flow regimes. *Journal of Fluid Mechanics*, *897*. https://doi.org/10.1017/jfm.2020.371

Tahir, S. A. R., Virk, M. S., & Awoniyi, T. O. (2021). Offshore Wind Energy in Ice Prone Cold Regions - An Overview of Technological Gaps and Needs. *International Conference on Engineering and Emerging Technologies (ICEET)*, 1–6.

Wei, K., Yang, Y., Zuo, H., & Zhong, D. (2020). A review on ice detection technology and ice elimination technology for wind turbine. *Wind Energy*, *23*(3), 433–457.